Selective Activation of TASK-3-containing K^+ Channels Reveals Their Therapeutic Potentials in Analgesia

Ping Liao[1*], Yunguang Qiu[3,8*], Yiqing Mo[2*], Jie Fu[2*], Zhenpeng Song[1*], Lu Huang[1*], Suwen Bai[4], Yang Wang[4], Jia-Jie Zhu[5], Fuyun Tian[3], Zhuo Chen[1], Nanfang Pan[1], Er-Yi Sun[1], Linghui Yang[1], Xi Lan[3], Yinbin Chen[2], Dongping Huang[2], Peihua Sun[6], Lifen Zhao[3], Dehua Yang[3], Weiqiang Lu[2], Tingting Yang[7], Junjie Xiao[7], Wei-Guang Li[5], Zhaobing Gao[3], Bing Shen[4], Qiansen Zhang[2], Jin Liu[1], Hualiang Jiang[3,8], Ruotian Jiang[1†], Huaiyu Yang[2†]

[1]Laboratory of Anesthesia and Critical Care Medicine, Department of Anesthesiology, Translational Neuroscience Center, West China Hospital of Sichuan University, Chengdu 610000, Sichuan, China.

[2]Shanghai Key Laboratory of Regulatory Biology, Institute of Biomedical Sciences, School of Life Sciences, East China Normal University, Shanghai 200241, China.

[3]State Key Laboratory of Drug Research and CAS Key Laboratory of Receptor Research, Shanghai Institute of Materia Medica, Chinese Academy of Sciences, Shanghai 201203, China.

[4]Department of Physiology, Anhui Medical University, Hefei 230032, Anhui, China.

[5]Collaborative Innovation Center for Brain Science, Department of Anatomy and Physiology, Shanghai Jiao Tong University School of Medicine, Shanghai 200025, China.

[6]Jiangsu Key Laboratory of Neuropsychiatric Diseases and College of Pharmaceutical Sciences, Soochow University, Suzhou, Jiangsu 215123, China

[7]Cardiac Regeneration and Ageing Lab, School of Life Science, Shanghai University, Shanghai 200444, China.

[8]University of Chinese Academy of Sciences, Beijing 100049, China

* These authors contributed equally to this work.

†Corresponding authors. hyyang@bio.ecnu.edu.cn for H.Y.; ruotianjiang@scu.edu.cn for R.J..

ABSTRACT

The paucity of selective agonists for TASK-3, a member of two-pore domain K^+ (K2P) channels, limited our understanding of its biological functions. Targeting a novel druggable transmembrane cavity using structure-based drug design approach, we discovered a biguanide compound CHET3 as a highly selective allosteric activator for TASK-3-containing K2P channels including TASK-3 homomer and TASK-3/TASK-1 heteromer. CHET3 displayed unexpectedly potent analgesia *in vivo* in a variety of acute and chronic pain models in rodents that could be abolished by pharmacology or genetic ablation of TASK-3. We further found that TASK-3-containing channels anatomically define a unique subset population of small-sized, TRPM8, TRPV1 or Tyrosine Hydroxylase positive nociceptive sensory neurons and functionally regulate their membrane excitability, supporting the CHET3 analgesia in thermal hyperalgesia and mechanical allodynia under chronic

pain. Overall, our proof-of-concept study reveals TASK-3-containing K2P channels as a novel druggable target for treating pain.

One Sentence Summary: Identification of a novel drug target and its new hit compounds for developing new-generation non-opioid analgesics.

INTRODUCTION

Currently available analgesics do not treat pain completely and some of them, particularly opioids, provoke social problems (*1*). It is an urgent need to discover new therapeutic targets for developing new-generation analgesics. In particular, targets that treat a variety of pain with similar potency but less side effects compared to μ-opioid receptor are keenly awaited. In this regard, two-pore domain K^+ (K2P) channels hold great promise (*2*), since they produce background leak K^+ currents (*3*) and the activation of which in nociceptors theoretically inhibits pain signaling (*4-6*). The expression of TASK-3 (*Kcnk9*), a K2P channel, has been detected in peripheral and central nervous system (*7*, *8*) including in human dorsal root ganglia (*9*). Recent evidence suggested that TASK-3 is involved in perception of cold (*10*), and the variations in *Kcnk9* gene are associated with breast pain in breast cancer patients (*11*). However, its functional and anatomical involvement in chronic pain remain largely unknown. More importantly, the paucity of selective agonists limits the drug target validation of TASK-3, leaving the notion that

selective activation of TASK-3 alleviates pain hypothetical. Here we sought to discover selective activators for TASK-3 and to use the activators as tool compounds to reveal and the translational potentials and the underlying mechanisms of TASK-3 in treating pain.

RESULTS

Discovery of selective activator CHET3 for TASK-3-containing channels

We set out to discover selective activators for TASK-3 via structure-based virtual screening. Since no crystal structure of TASK-3 has been determined yet, we sought to build a structural model using homology modeling. Firstly, a crystal structure was chosen as the template. To this end, Fpocket 2.0 server (*12*) was applied to detect pockets in the reported crystal structures of K2P channels. In this computation, druggability score more than 0.5 (the threshold) means the pocket might be druggable. We found that the cavity under the intracellular side of the filter and the nearby crevice between TM2 and TM4 in four crystal structures (with PDB codes 4RUE, 3UKM, 4XDK and 4XDL) (*13-15*) have druggability scores more than 0.5 (fig. S1).Thus, this cavity may be a drug binding pocket. Among the four crystal structures, the structure of TREK-2 channel (PDB code 4XDL) is a suitable template for building the structural model of TASK-3, because this structure has good sequence identity (31%) and expectation value (3E-32) in the sequence alignment generated using BLAST program (blastp algorithm) and Clustal Omega server (*16, 17*). Moreover, this TREK-2 structure stood out from the template

84 searching results (with the best QSQE value: 0.66) in SWISS-MODEL server (*18, 19*).
85 Thus, the structural model of TASK-3 was built based on this crystal structure with
86 Modeller (*20*). Then, based on this model, we performed virtual screening targeting the
87 pocket (Fig. 1, A and B) with SPECS and ChemBridge databases. A few hits were
88 selected for the whole-cell patch-clamp electrophysiological tests in HEK-293 cells
89 overexpressing recombinant human TASK-3, which led to the discovery of a biguanide
90 compound CHET3, a novel TASK-3 activator (half-maximum effective concentration
91 (EC_{50}) 1.4 ± 0.2 μM, Fig. 1, C to F). CHET3 enhanced TASK-3-mediated K^+ currents
92 maximally by ~4-fold which can be reversed by washout (Fig. 1D) or with
93 pharmacological blockade by PK-THPP (86 ± 3% inhibition at 0.5 μM, n = 6 cells,
94 representative traces shown in Fig. 1E), a TASK-3 specific inhibitor (*21*). In
95 single-channel recordings by inside-out patches, CHET3 enhanced the channel openings
96 mediated by TASK-3 (Fig. 1, G to K), further supporting that CHET3 directly activated
97 TASK-3. Increases in open probability and conductance were observed in both the inward
98 and outward directions in response to 3 μM CHET3 (Fig. 1, I to K).

99 In addition to forming homomer channels, TASK-3 subunit can efficiently form
100 heteromer channels with TASK-1 subunit (*22*). Electrophysiological assays showed that
101 CHET3 could activate TASK-3/TASK-1 (*23, 24*) with an EC_{50} value of 2.5 ± 0.2 μM
102 with a reduced maximal efficacy of ~2.4 fold (Fig. 1F), which were also blocked by
103 PK-THPP (90 ± 2% inhibition at 0.5 μM, n = 5 cells, representative traces shown in fig.

S2A). However, CHET3 did not activate TASK-1 channels up to 10 μM (Fig. 1F and fig. S2B). Thus CHET3 is an activator specific for TASK-3 homomer and TASK-3/TASK-1 heteromer, two TASK-3-containing channels, with high selectivity against the structurally most related K^+ channel TASK-1. In the subsequent sections, we use TASK-3-containing channels to represent TASK-3 homomer and TASK-3/TASK-1 heteromer.

Next, we further examined the selectivity of CHET3. Electrophysiological assays on several other K2P channels, including TREK-1, TREK-2, TRAAK, TRESK and THIK-1, further supported that CHET3 has high subtype selectivity among the K2P family (Fig. 1L and fig. S2B). Further, we found that 10 μM CHET3 has high selectivity against human ether-à-go-go–related gene (hERG) channel, voltage-gated K^+ channel subfamily B member 1 (Kv2.1), large conductance Ca^{2+}-activated K^+ channel (BK), three K^+ channels sharing similarity with K2P in filter structure and dynamics (*25*), and transient receptor potential cation channel subfamily M member 8 (TRPM8) and transient receptor potential cation channel subfamily V member 1 (TRPV1) (Fig. 1M, fig. S2, C to G).

We also excluded agonizing and antagonizing functions of CHET3 on pain-related G protein-coupled receptors (GPCRs) by testing the cellular function of μ-opioid receptor (μOR), 5-hydroxytryptamine receptor 1B ($5\text{-}HT_{1B}R$) and cannabinoid receptor type 1 (CB_1R) upon 10 μM CHET3 (fig. S3). Collectively, these results indicate that CHET3 is a selective activator of TASK-3-containing channels.

Activation mechanism of CHET3

Binding models derived from docking simulation were optimized by molecular dynamics (MD) simulations (fig. S4), which revealed the predominant binding mode of CHET3 within the pocket (Fig. 2, A and B). We next examine the ligand-channel interactions in this binding mode using mutagenesis experiments and RosettaLigand (*26, 27*). Residues T93 and T199 indirectly interacts with CHET3 by water bridges (Fig. 2, A and B). The two residues belong to the filter region, and the mutations T93A and T199A led to non-functional channels (fig. S5, A and B). F125 may form a π-π interaction with CHET3, and other surrounding residues, including I118, F125, T198, L232, I235, F238 and L239, likely contribute hydrophobic interactions with the ligand. RosettaLigand computations based on this MD mode predicted that the I118A, F125A, L232A, I235A, F238A and L239A mutants decrease CHET3 binding, while the T198A mutant should not (Fig. 2C). Indeed, a saturating concentration of CHET3 (10 μM) showed no activation on the mutants of F125A, I235A, F238A and reduced activation on mutant L239A, whereas CHET3 did activate T198A similarly to the WT (Fig. 2D). Mutant L232A is non-functional (fig. S5C). Although CHET3 did not show reduced activation on I118A (Fig. 2D), the experimental results are generally consistent with the computational predictions. To gain further insights into action mechanism of CHET3, MD simulations were carried out on the *apo* TASK-3 to compare with the CHET3-bound TASK-3 (Fig. 2, E and F). In two out of three independent simulations for the *apo* system, the channel selectivity filter tended to stay in a nonconductive-like conformational state (Fig. 2, E and

144 F). By contrast, in all the three simulations for the CHET3-bound system, the channel
145 filter adopted a conductive-like state (Fig. 2, E and F). Further, our simulations supported
146 the previous report by González *et al.* that the residue H98 plays roles in modulating the
147 extracellular ion pathway in TASK-3 (*28*). In the simulations of the CHET3-bound
148 TASK-3, H98 adopted a conformation to open the extracellular ion pathway (Fig. 2E and
149 fig. S6A). By contrast, in ligand-free mode, H98 has a high probability to adopt a
150 conformation to close this pathway (Fig. 2E and fig. S6B).

151 **CHET3-induced analgesia in rodents**

152 Next, we evaluated CHET3 in analgesia systematically. The anti-nociceptive effect of
153 CHET3 was firstly assessed by the tail immersion test at 52 ℃. CHET3 displayed
154 dose-dependent analgesia with a fast onset (30 min) after intraperitoneal (i.p.) injection
155 with a maximal effect at a dose of 10 mg/kg (Fig. 3A). Hereafter, i.p. injection with 10
156 mg/kg was used for most of the following animal studies. Interestingly, CHET3 was only
157 effective in response to a noxious cold stimulus (5 ℃) or noxious heat stimuli (46 ℃ and
158 52 ℃) but not to physiological stimuli (20 ℃ and 40 ℃) (Fig. 3A). Importantly, the
159 CHET3 analgesia was fully blocked by the co-administration of PK-THPP, and PK-THPP
160 alone also produced nociceptive effect in tail immersion test at 46 ℃ (Fig. 3A). Next,
161 both the early and the late phases (*29*) of acute inflammatory pain induced by formalin
162 were attenuated by CHET3 (Fig. 3B), suggesting at least a peripheral effect of CHET3.
163 CHET3 reduced mechanical pain revealed by paw pressure test in mice, and the effect

was fully blocked by PK-THPP (Fig. 3C). Next, we evaluated the analgesic effects of CHET3 on chronic pathological pain. In the spared nerve injury (SNI)-induced neuropathic pain mouse model, CHET3 significantly reduced the frequency of hind paw lifting (Fig. 3D), an indicator of spontaneous/ongoing pain behavior in SNI model (*30*). In the cold plantar test, CHET3 attenuated the cold hyperalgesia in SNI at the development (SNI 7 d) and maintenance (SNI 14 d and 21 d) stages of the chronic pain, which could be reversed by PK-THPP. PK-THPP alone, however, had no effect in cold plantar test in SNI mice (Fig. 3E). Compared to Pregabalin, a first line agent for the treatment of neuropathic pain, CHET3 was more effective in relieving cold hyperalgesia (Fig. 3F). In SNI mice, CHET3 has little effect on alleviating mechanical allodynia in the von Frey test. However, in SNI rats, CHET3 at the dose of 10 mg/kg attenuated the mechanical allodynia throughout the different stages of the chronic pain in the von Frey test, which could be reversed by PK-THPP (Fig. 3G). PK-THPP alone had no effect in the von Frey test in SNI rats (Fig. 3G). The analgesic effect of CHET3 at the dose of 20 mg/kg exhibited a faster onset (30 min post injection) with similar efficacy compared to these at 10 mg/kg (fig. S7) in the von Frey test in SNI rats. In chronic inflammatory pain induced by the Complete Freund's Adjuvant (CFA), CHET3 reduced heat hyperalgesia in the Hargreaves test, which was blocked by PK-THPP (Fig. 3H). In addition, PK-THPP injection alone aggravated heat hyperalgesia (Fig. 3H).

Chronic pain may induce anxiety (*31, 32*). Compared with the Sham group, the SNI

mice spent less time in open arms in the elevated plus maze test, and spent less time in the light box in the light/dark box test, suggesting anxiety-like behaviors in the SNI mice. Administration of CHET3 30 min before the test significantly alleviated anxiety-like behaviors in both tests (Fig. 3, I and J). Together, our data suggest CHET3 potently and efficaciously attenuated acute and chronic pain and pain-associated anxiety in rodents, and the analgesic effects of CHET3 can be pharmacologically blocked by the TASK-3 blocker PK-THPP. Importantly, CHET3 was inactive in grip strength, rotarod and open field tests (fig. S8, A to C), suggesting that CHET3 had no effect on the locomotion activities in mice. Since TASK-3 was found to be expressed in mouse carotid boy type-1 cells (*33*), we also evaluated the possible side effects of CHET3 on the cardiovascular functions in mice or rats. We monitored the blood pressure as well as heart functions using echocardiography, and we did not observe any significant change in blood pressure (fig. S8, D to F) or heart functions including Ejection Fraction (EF) and Fractional Shortening (FS) (table S1) in a post-injection time window between 45 min–90 min where CHET3-induced analgesia peaked in most cases. We also monitor the body temperature change following CHET3 systemic administration, and no significant hyperthermia or hypothermia was observed (fig. S8G).

Further on-target validation using chemical and genetic approaches

Was CHET3 truly targeting TASK-3 containing K^+ channels to be analgesic? We then performed additional target validation experiments using chemical and genetic

204 approaches. Medicinal chemistry yielded CHET3-1 and CHET3-2 (Fig. 4A), two
205 derivatives of CHET3. In the CHET3-TASK-3 binding model (Fig. 2, A to B), the
206 dioxane ring may form a π–π interaction with the residue F125. CHET3-1, where the
207 dioxane ring was replaced with an aromatic ring, should keep the π–π interaction.
208 CHET3-2 should lose it since the dioxane was replaced by a steric bulk *tert*-butyl group.
209 Binding energy computations based on the binding model suggested that the binding
210 affinity of CHET3-1 to TASK-3 was similar with CHET3, while that of CHET3-2 should
211 decrease (fig. S9). In accord, CHET3-1 activated TASK-3 with an EC_{50} value of 0.5 ± 0.1
212 μM, while CHET3-2 was inactive (Fig. 4B), further supporting the putative binding
213 model. We reasoned that CHET3-1 should be bioactive in analgesia whereas CHET3-2
214 should not, if CHET3 truly targets TASK-3-containing channels to be analgesic. Indeed,
215 CHET3-1 attenuated cold hyperalgesia in SNI mice (Fig. 4C) and mechanical allodynia
216 in SNI rats (Fig. 4D), and heat hyperalgesia in CFA mice (Fig. 4E), all these effects could
217 be reversed by PK-THPP (fig. S10). In contrast, CHET3-2 was completely inactive in all
218 the experiments above (Fig. 4, C to E).

219 We generated the *Kcnk9* gene knockout (TASK-3 KO) mice (fig. S11). Knocking out
220 *Kcnk9* should abolish the function of TASK-3 homomer and TASK-3/TASK-1 heteromer
221 *in vivo*. In the TASK-3 KO and their WT control mice, we measured the basal sensitivity
222 to nociception, thermal hyperalgesia and mechanical allodynia, and we also evaluated the
223 analgesic effect of CHET3 in these mice. Tail immersion (Fig. 5, A and B), paw pressure

tests (Fig. 5C) or von Frey tests in naive animals (Pre SNI, Fig. 5D) did not reveal any significant difference in baseline nociceptive sensitivity between TASK-3 KO and WT; however, cold plantar (Pre SNI, Fig. 5F) and Hargreaves tests (Pre CFA, Fig. 5G) revealed increased nociceptive cold and heat sensitivity in TASK-3 KO mice. Furthermore, in the chronic pain models, von Frey, cold plantar and Hargreaves tests revealed that TASK-3 KO mice exhibited aggravated mechanical allodynia (Fig 5D), spontaneous neuropathic pain behavior (Fig. 5E), and thermal hyperalgesia (Fig. 5, F and G). CHET3, as expected, in TASK-3 KO mice, was completely inactive in all the tests described above (Fig. 5, A to G). Thus, using tool compounds (Fig. 4) and mouse genetics (Fig. 5), we provided strong evidence to show that CHET3 targets TASK-3-containing channels to be analgesic, and the loss of TASK-3 contributed to the generation/maintenance of both acute and chronic pain.

Distribution of TASK-3-containing channels in sensory neurons

Our pharmacokinetic profile of CHET3 (table S2) showed a negligible brain concentration (C_{max} = 79.1 ng/mL) of CHET3 and a high concentration in the plasma (C_{max} = 1112.0 ng/mL), suggesting CHET3 mainly acted peripherally. The peripheral effect of CHET3 was also supported by the fact that CHET3 attenuated the early phase of formalin-induced pain (Fig. 3B). These along with the previous finding that TASK-3 in dorsal root ganglion (DRG) neurons mediates cold perception (*10*) together strongly suggest that peripheral TASK-3-containing channels contribute largely, if not all, to

CHET3 analgesia. Therefore, we evaluated the TASK-3 functions/distributions in peripheral nervous system, particularly in DRG.

We used fluorescence in situ hybridization (ISH) (RNAscope technique) to map the mRNA expression of TASK-3 in DRG and trigeminal ganglia (TG). The specificity of the fluorescent signals was validated by positive control probe and negative control probe (see methods). *Kcnk9* was identified in a subset of neurons (~7% of total neurons) in DRG, predominantly in small-sized neurons (diameter $\leq$ 20 μm) (Fig. 6, A and C), indicative of its specific expression in nociceptors. Interestingly, in TG, a much higher expression level of *Kcnk9* (~14% of total neurons) was found (Fig. 6, A and B). In DRG, approximately 95% of *Kcnk9*$^{+}$ neurons express TASK-1 subunit, suggesting a possible formation of TASK-3/TASK-1 heteromer in DRG, and approximately 50% of *Kcnk9*$^{+}$ neurons express TRPV1, a well-known noxious heat sensor predominantly expressed in peptidergic nociceptive sensory neurons (*34*). More than 95% of *Kcnk9*$^{+}$ neurons express TRPM8, and very little *Kcnk9*$^{+}$ neurons express TRPA1, two well-known noxious cold sensors (*34*). Further, approximately 50% of *Kcnk9*$^{+}$ neurons express Tyrosine Hydroxylase (TH), a marker for c-low threshold mechanoreceptors (c-LTMRs) predominantly found in non-peptidergic nociceptors (*35*), whereas *Kcnk9* rarely colocalized with *P2rx3* (P2X3), which labels mainly TH^{-} negative, IB4^{+} non-peptidergic nociceptors (*36*), nor did they colocalize with *Ntrk2* (TrkB) a marker for Aδ-LTMRs (*35*). Thus, TASK-3 marks a unique subpopulation of both peptidergic and non-peptidergic

nociceptive sensory neurons enriched in thermal sensors (TRPV1, TRPM8) or mechanoreceptors (TH^+ c-LTMRs) (Fig. 6, D to F), in line with its functional involvement in thermal and mechanical sensation *in vivo*. In line with the previous study (*37*), we found that *Kcnk9* expression was down regulated in SNI mice and CFA mice (fig. S12), further suggesting the down-regulation of TASK-3-containing channels contributes to the generation/maintenance of chronic pain.

Functional roles of TASK-3-containing channels in nociceptive neurons

The functional roles of TASK-3-containing channels were examined by whole-cell patch-clamp recordings in dissociated DRG neurons. Recordings were focused on small sized DRG neurons (diameter of ~20 μm, cell capacitance of ~30 pF) based on the ISH data. To isolate K^+ currents, the voltage ramps from -120 mV to -30 mV were applied. In total 89 cells recorded, 16 cells responded to CHET3 (20.3 ± 6.3%, 11 mice). In the CHET3-sensitive cells, CHET3 enhanced the whole cell current density by approximately 18%, which could be further inhibited by PK-THPP by approximately 38% at -30 mV (Fig. 7A). We subtracted the CHET3-sensitive current, and we found this current was strongly outwardly rectifying, and was tiny between -120 mV and -60 mV, leaving the reversal potential of the CHET3-sensitive current difficult to be resolved (Fig. 7B). We further sought to isolate current carried by TASK-3-containing channels by subtracting PK-THPP-sensitive current, and consistently, we found a similar profile for PK-THPP-sensitive current (fig. S13A), further suggesting the low basal conductance at

the hyperpolarized membrane potentials and strong outwardly rectifying represents an intrinsic property of K^+ currents mediated by TASK-3-containing channels in DRG under our experimental conditions. To increase the drive force of the K^+ currents in the hyperpolarized potentials, we increased the extracellular K^+ concentration to 143 mM. Under this condition, the CHET3-sensitive current was reversed at around 6.7 mV, which was close to the theoretical value of 1.5 mV for K^+ conductance (Fig. 7B).

The tiny CHET-3- or PK-THPP-mediated currents around -60 mV suggests that the basal activity of TASK-3-containing channels around the resting membrane potentials (RMP) range was low, and thus that CHET3 or PK-THPP was unlikely to be able to regulate the RMP. To systematically evaluate the regulatory role of CHET3 on the excitability of nociceptive neurons, first, we applied a cocktail solution containing Menthol and Capsaicin, two agonists for TRPM8 and TRPV1, respectively, to better identify the nociceptive neurons that likely express TASK-3-containing channels. Only neurons responding to the cocktail (fig. S13B) were furthered studied in the following experiments. Consistent with low activity of TASK-3-containing channels around -60 mV, application of CHET3 or PK-THPP or Vehicle (Control) did not hyperpolarize the RMP, rather, they all slightly depolarized it by ~2 mV with no significant difference among the three groups, suggesting CHET3 or PK-THPP had no specific roles in altering RMP (Fig. 7C). Next, we explored how CHET3 regulates action potentials. In 12 out of 27 neurons, application of CHET3 markedly increased by ~70% the rheobase required for eliciting

the action potentials (APs) and decreased by ~65% the frequency of APs evoked by suprathreshold current injections (Fig. 7, D and E), whereas in the other 15 cells, CHET3 had no effect on the rheobase and slightly increased by 10% the frequency of APs evoked by suprathreshold current injections (fig. S13, C and D). In 7 out of these 12 CHET3-sensitive cells, we were able to further apply PK-THPP, which reversed the effects of CHET3 (fig. S13, E and F). Furthermore, in another independent set of experiment, we co-applied CHET3 and PK-THPP in naive cells. In 11 out of 27 cells, the co-application of CHET3 and PK-THPP markedly decreased by ~40% the rheobase and increased by ~50% the frequency of APs evoked by suprathreshold current injections (Fig. 7, F and G), whereas in the other 16 cells, co-application of CHET3 and PK-THPP slightly increased the rheobase by ~20% but had no effect on the APs frequency evoked by suprathreshold current injections (fig. S13, G and H). Collectively, our electrophysiological data suggest the functional presence of K^+ currents mediated by TASK-3-containing channels, and the enhancement of which reduces the excitability of nociceptive neurons without affecting the RMP.

Last, Ca^{2+} imaging experiments were performed in acutely dissociated DRG neurons to measure how the activation of TASK-3-containing channels contributes to the thermal sensitivity of DRG neurons. Thermal stimulations elicited Ca^{2+} signals in a portion of small-sized DRG neurons (Fig. 7H, cells having ratio $F_{340}/F_{380} \geq 0.2$ were considered as responding cells shown in black, and those having ratio $F_{340}/F_{380} < 0.2$ were considered as

non-responding cells shown in grey). We confirmed that these Ca^{2+} signals were temperature-dependent and were mediated by TRP channels as the heat-induced responses can be blocked by 5 μM AMG9810 (TRPV1 antagonist) (fig. S14, A and B), and the cool-induced responses can be blocked by 10 μM BCTC (TRPM8 antagonist) and 20 μM HC030031 (TRPA1 blocker) (fig. S14, A and B). Bath application of 10 μM CHET3 significantly and markedly inhibited the Ca^{2+} signals evoked by cool- or heat-stimulations in small-sized DRG neurons (Fig. 7, H and I), suggesting the activation of TASK-3-containing channels was able to lower the excitability of the nociceptive neurons in response to external thermal stimulations.

DISCUSSION

The current study has three major findings: first, we discovered selective agonists for TASK-3-containing channels by targeting a transmembrane cavity under the selectivity filter using the structure-based approaches. Second, *in vivo* activation of peripheral TASK-3-containing channels displayed potent analgesia, suggesting a TASK-3-based therapeutic strategy for treating chronic inflammatory and neuropathic pain. Third, our anatomical and functional data highlight the roles of peripheral TASK-3-containing channels in controlling the excitability of nociceptive neurons.

Very recently, Schewe *et al.* reported a class of negatively charged activators (NCAs) that could activate K2P channel, hERG channel and BK channel and revealed that the site

344 below the selectivity filter is the binding site of the NCAs (*25*). In the present work we
345 obtained CHET3 acting on this site, a non-charged compound, by virtual screening,
346 further supporting the finding that the site below the selectivity filter is a ligand binding
347 site. It is noteworthy that NCAs are non-selective activators for a variety K^+ channels
348 while CHET3 is highly selective for TASK-3-containing channels, suggesting the
349 versatility of this binding site. Plus, NCAs and CHET3 may share some common
350 activation mechanisms on K2P channels by both influencing the conformation of
351 selectivity filter. Notably, the activation mechanism we provided in this study could not
352 fully explain the selectivity of CHET3 at present. In particular, TASK-1 and TASK-3 are
353 closest relative to each other, and the residues below selectivity filter are conserved as
354 well as H98. Further studies to elucidate the differential responses of TASK-1 and
355 TASK-3 to CHET3 may be helpful for understanding the selective modulation principle
356 in K2P.

357 In most cases, the initial proof-of-concept identification of a protein as a potential
358 target is dependent on genetic methods. However, genetic deletion may produce
359 modifications on other genes. This off-target genetic side effects discredit target
360 validation work. This is particularly the case in the field of pain medicine: genetically
361 mutated mice, e.g., $Na_v1.7$-null mice, or human exhibited remarkable insensitivity to pain,
362 whereas potent selective antagonists have weak analgesic activity (*38, 39*). Another
363 example more related to K2P field is that migraine-associated TRESK mutations lead to

the inhibition of TREK-1 and TREK-2 through frame shift mutation-induced alternative translation initiation (fsATI) to increase sensory neuron excitability and is linked to migraine (*40*). Using chemical probes to validate targets pave another way for the later translational research. For in *vivo* applications of chemical probes in target identification and validation, a major issue is whether the observed phenotypes are indeed relevant to the on-target of the probes. In this study, we provided three independent lines of evidence to show CHET3 targets TASK-3-containing channels to be analgesic. First, TASK-3 inhibitor PK-THPP could block the CHET-3 induced analgesia. Second, two structurally highly close analogs were discovered and used in *in vivo* tests. CHET3-1, a TASK-3 activator structurally highly close to CHET3, is bioactive in analgesia, which could be also blocked by PK-THPP. CHET3-2, another analog structurally highly close to CHET3 inactive on TASK-3, was completely inactive in all the analgesia tests. Last, CHET3 was completely inactive in analgesia in TASK-3 KO mice in all the tests. Collectively, our data suggest that the on-target activity of CHET3 links to the analgesic phenotypes.

Although CHET3 has a higher activation efficacy on TASK-3 over TASK-3/TASK-1, we suggest that both TASK-3 homomer and TASK-3/TASK-1 heteromer channels likely contribute to CHET3-induced analgesia based on the following reasons: 1) *Kcnk9* is highly colocalized with *Kcnk3* in DRG; 2) TASK-3/TASK-1 heteromer has been found assembled efficiently and functionally in cerebellar granule cells (*41*), motoneurons (*42*) and carotid body glomus cells (*43*).

We found that CHET3 decreased the excitability with no change in RMP of the nociceptive neurons. No change of RMP could be well explained by the fact that CHET3-or PK-THPP-mediated currents are negligible around –60 mV. One may argue that there may be a strong depolarizing "off-target" activity of CHET3 through another unknown channel/receptor, thereby masking the hyperpolarizing effect mediated by CHET3 on TASK-3 containing channels. However, if this were the case, one would at least expect PK-THPP to depolarize the RMP, since PK-THPP, a molecule structurally distinct to CHET3, is unlikely produce the hyperpolarizing "off-target" activity through the same unknown channel/receptor.

CHET3 acted mainly on peripheral TASK-3-containing channels. Peripheral targets are much less likely to produce central side effects including dependence/addiction. Although the utility of CHET3 and its derivatives as pre-clinical candidate compounds require to be further assessed with systematically non-clinical safety tests performed in GLP (Good Laboratory Practice) in rodents and other animals, it seems that the activation of peripheral TASK-3-containing channels does not produce obvious severe acute side effects on cardiovascular system where TASK-3-containing channels were also expressed. Interestingly, we found that TASK-3 was expressed in TG with a higher expression rate than DRG. Further studies are needed to evaluate the translational potentials of activation TASK-3 (TASK-3/TASK-1) in TG to treat chronic pain related to trigeminal neuralgia and migraine. Last, although TASK-3 was found expressed in human DRG (*9*) and

404 variation of *KCNK9* was involved in breast pain in breast cancer patients (*11*), direct
405 evidence for functional involvement of TASK-3 in pain signaling in human remains
406 lacking. Future functional studies on human tissues or studies with genetic screening of
407 TASK-3-related mutations in human would greatly aid the assessment of the translational
408 potential of TASK-3 in treating pain in human.
409

410 **MATERIALS AND METHODS**

411 **Study design**

412 Structure-based drug design methods were used to perform initial virtual screening and
413 patch-clamp electrophysiology was mainly used to study the activity/mechanism of
414 candidate compounds on TASK-3-containing channels. Analgesic effects of TASK-3
415 activators were then studied in acute and chronic pain models in mice and rats.
416 Pharmacokinetic analysis was performed to assess how CHET3 was distributed. KO mice
417 were used to confirm the on-target activity of CHET3. Last, *in situ* hybridization with
418 RNAscope technique was used to map the distribution of TASK-3 in DRG and TG. The
419 functional roles of TASK-3 were assessed by measuring how CHET3 and PK-THPP
420 modulate the K^+ currents, action potential firings and sensitivities to thermal stimulations
421 in nociceptive neurons.

422 Sample size and replicates: For mutations of TASK-3 led to no-functional currents, 3
423 cells per mutation were tested. For other studies of ion channels in cells including these in

cell line system and acutely prepared DRG cells, at least 5 cells per condition were tested. For experiments in DRG neurons, at least 3 independent preparations of DRG culture were performed. For in *vivo* studies with animals, 6-10 animals per condition were used. No power analysis was performed to determine the sample size.

Homology modeling for TASK-3 structure

Sequence alignment was generated by using Clustal Omega server (*16*). Notably, the two pore domain and selectivity filter sequence motif were highly conserved among the K2P channels, which were largely used to guide the alignment. Conserved residues E30 and W78 in TASK-3 helped to locate the position of non-conserved cap domain.

Virtual screening

Docking was performed by using Schrödinger Glide software (New York, NY, USA). Compounds were screened using the high-throughput virtual screening (HVS) module followed by a standard docking module SP in Glide. Glide G-score was used to rank the result list. Allowed for diversities of molecule structure, binding mode and drug-like properties, twelve hits were selected for bioassay.

Chemicals

PK-THPP was purchased from Axon Medchem. CHET3 purchased from commercial sources was used in the initial electrophysiological screening. Then CHET3 was synthesized in the lab for the following studies in this paper. Synthesis routes and characterization of CHET3 and its derivatives CHET3-1 and CHET3-2 are outlined in the

Supplementary Materials.

For electrophysiology, stock solutions of CHET3 and derivatives (50 mM) were prepared in dimethyl sulfoxide (DMSO) and diluted in the extracellular solution before use.

For animal studies, CHET3 and PK-THPP were both dissolved in 10% DMSO, 5% tween80 and 85% saline, CHET3-1 was dissolved in 10% DMSO, 5% Castor Oil Ethoxylated, 35% Poly (Ethylene Glycol) and 50% corn oil, and CHET3-2 was dissolved in 14% DMSO, 5% tween80 and 81% saline. The solvents were used as vehicle controls.

Detailed modeling of the CHET3-TASK-3 binding poses

Initially, the configuration of CHET3 was determined by Ligprep module in the Schrödinger Maestro and Gaussain09 (Gaussian, Inc). Detailed descriptions are displayed in the Supplementary Materials. The configuration of tautomer with lowest energy was adopted to generate multiple ring conformations. CHET3 conformations were docked to the TASK-3 channel model by standard Glide as described for the virtual screening. Two binding modes (G-score values at -8.3 and -7.9, separately) were obtained from docking. In the best pose (1^{st} model in fig. S4A), the guanidyl group in CHET3 establishes hydrogen bond with backbone NH of L232 residues in TM2, while the guanidyl group in the additional mode of binding (2^{nd} model in fig. S4B) faces towards the selectivity filter and interacts with hydroxyl group of T199. To identify the accurate binding mode of CHET3, two models from docking were further studied using molecular dynamics (MD)

simulations (see below).

MD simulations

The TASK-3 model obtained from the homology modeling and two binding models of CHET3-bound TASK-3 were used to build the models of the *apo* TASK-3 and the CHET3-bound TASK-3, respectively. Models were inserted in a POPC (1-palmitoyl-2-oleoyl-sn-glycero-3-phosphocholine) lipid bilayer to establish the CHET3-bound system and the *apo* system, respectively. MD simulations were carried out by using GROMACS 5.1.4 (*44*) with CHARMM36 parameters (*45*).

Comparison of the binding of CHET3, CHET3-1 and CHET3-2

RosettaLigand application (*26, 27*) was applied to dock CHET3, CHET3-1 and CHET3-2. The best binding mode obtained from MD simulations were adopted as the initial docking model. For each docking trial, top 1000 models were sorted by total score and the binding energy between three compounds and the channel were calculated. Also, *in silico* alanine scan were conducted by individually changing residue to alanine without otherwise changing the conformation of protein or ligands in Rosetta. To explore the distribution of binding interactions between compounds and proteins, the average energy of top 10 models with the lowest binding energies (interface score) were calculated. To compare the binding of CHET3, CHET3-1 and CHET3-2, top 50 models of each compound with the lowest binding energies were used to calculate the total score and interface score.

Electrophysiology

Electrophysiology tests of hTASK-3, hTASK-1, hTREK-1, mTREK-2, hTRAAK, hTHIK-1, hTRESK, hTASK-3/hTASK-1, hTRPM8 and hTRPV1 were done with transiently transfected HEK-293T cells. The cDNA of hTASK-3, hTASK-1, hTHIK-1, hTRESK and hTASK-3/hTASK-1 were subcloned into the pCDNA3 vector (Invitrogen). The cDNA of hTREK-1, mTREK-2, hTRAAK, hTRPM8 and hTRPV1 were subcloned into the pEGFPN1 expression vector (Invitrogen). For the hTASK-3/hTASK-1 concatemer products were designed for the 3' and 5' ends of TASK-3 and TASK-1 ensuring that the stop codon of TASK-3 was removed.

Electrophysiology tests of hERG, Kv2.1 and BK were done with stable cell lines. The CHO-hERG stable cell line was generated in-house and was based on a standard CHO-K1 cell line. The HEK293-human Kv2.1 stable cell line and the CHO-human BK stable cell line were generated by Ion Channel Explore (Beijing, China).

Whole-cell recordings of ion channels were performed with patch-clamp amplifiers (EPC10, HEKA or Axon 700B, Molecular Devices) at 23-25 ℃. The current signals were filtered at 2 kHz and digitized at 10 kHz. The pipettes for whole cell recordings were pulled from borosilicate glass capillaries (World Precision Instruments) and had a resistance of 3-7 MΩ. For recordings of K^+ channels, the standard pipette solution contained (in mM): 140 KCl, 2 $MgCl_2$, 10 EGTA, 1 $CaCl_2$, 10 HEPES (pH 7.3, adjusted with KOH), and the external solution contained (in mM): 150 NaCl, 5 KCl, 0.5 $CaCl_2$, 1.2 $MgCl_2$, 10 HEPES (pH 7.3, adjusted with NaOH). For recordings of the TRPV1 and

TRPM8 currents, the internal solution contained (in mM): 140 CsCl, 0.1 $CaCl_2$, 1 $MgCl_2$, 10 HEPES, 5 EGTA (pH 7.2, adjusted with CsOH), and the external solution contained (in mM): 140 NaCl, 5 KCl, 1 $MgCl_2$, 0.5 EGTA, 10 HEPES (pH 7.4, adjusted with NaOH). For recordings of hERG, the outward current of hERG channels was elicited by a 2.5-second depolarization step to +30 mV from a holding potential of -80 mV followed by a 4-second repolarization step to -50 mV to measure the tail current. For recordings of Kv2.1, currents were evoked by a 200-millisecond depolarization step to +60 mV from a holding potential of -80 mV. For recordings of BK, currents were evoked by a 1-second depolarization step to +70 mV from a holding potential of -80 mV. For recordings of TRPV1 and TRPM8, currents were recorded using a ramp protocol from -100 mV to +100 mV over a period of 400-millisecond at a holding potential of 0 mV.

Inside-out patches were done by using EPC10 (HEKA) at 23-25 °C. The pipettes for single-channel recordings had resistances of 7-15 MΩ. The standard pipette and bath solutions contained (in mM): 140 KCl, 1 $CaCl_2$, 2 $MgCl_2$, 10 HEPES, 10 EGTA (pH 7.4, adjusted with KOH). Currents were recorded at a pipette potential of -60 mV and +60 mV respectively.

Ethics statement

All experiments with animals were approved by the Animal Research Committee of East China Normal University (PROTOCOL No.: m20171020 and m20180112) and the Animal Research Committee of West China Hospital of Sichuan University

(PROTOCOL No.: 2018175A). For tissue collection, mice were given a lethal dose of pentobarbital intraperitoneally.

Animals

BALB/c mice and Sprague-Dawley rats were used in most animal studies, and TASK-3 KO mice and WT control littermates were on a C57BL/6 background. Male mice or rats aged 8-10 weeks were used for behavior tests, unless stated otherwise. Animals were housed in a conventional facility at 21 ℃ on a 12 h light-dark cycle with unrestricted access to food and water.

TASK-3 KO mice generation

To generate a *Kcnk9* knockout C57BL/6 mouse line by CRISPR-Cas9 genome editing system, two single-guide RNAs (sgRNA-1, 5′-CCGCTTCATGGCCGCGAAGAAGG-3′, and sgRNA-2, 5′-AGGAACCGGCGAATTTCCACTGG-3′) flanking exon1 were designed (Bioray Laboratories). A 241-bp deletion was bound to the exon 1 of the *Kcnk9* gene locus, resulting $Kcnk9^{\Delta/\Delta}$ mice with a frameshift mutation. Additional information is provided upon request.

Spared nerve injury model

Unilateral spared nerve injury (SNI) surgery was performed. The experiment animal was laid on prone position. After disinfection with povidone iodide and 75% ethanol, a minimal skin incision is made at the mid-thigh level in order to exposing the sciatic nerve and its three branches via separating the muscle layers. The tibial and common peroneal

nerves were tightly ligated with 5.0 silk threads and a 1-2 mm length section was removed between the proximal and distal parts of nerves. The sural nerve was restrictively preserved to avoiding any harmful injury. The muscle layer and skin were closed after surgery and animals were transferred to a warm pad to recover from anesthesia.

Chronic inflammatory pain model

A volume of 20 μL Complete Freund's Adjuvant (CFA) (Sigma-Aldrich) was subcutaneously injected into the left hindpaw of mouse to induce chronic inflammatory pain in mouse. After injection the syringe was maintained for at least 30 s to avoid overflow.

Tail immersion

Mice were restrained in the test tube with the tails stretching out and moving freely 15 min twice daily for 3 days. The distal third tails were immersed into a water bath at 5 ℃, 20 ℃, 40 ℃, 46 ℃, or 52 ℃. The three measurements of tail flick latency (in second) to stimulation as indicated by rapid tail flexion were averaged. A cutoff value of 15 seconds was adopted to prevent unexpected damage.

Formalin test

Mice were housed individually in Plexiglas chambers, after habituation to the testing environment for at least 30 min, the left hindpaw of the mice were injected subcutaneously with formalin (20 μL of 2.5% formalin, diluted in saline) and the mice

were put into the chamber of the automated formalin apparatus where movement of the formalin-injected paw was recorded by an action camera (SONY, HDR-AS50). The number of paw flinches was counted at 5 min intervals for 60 min by a blind experimenter. Time spent exhibiting these pain behaviors was recorded for the first (0-10 min) and second phases (10-60 min).

Paw pressure

The effects of the mechanical nociception were evaluated with an Analgesimeter (model 37215; Ugo-Basile, Varese, Italy). Mice were placed in the testing room for 3 continuous days to acclimate environment. The hindpaw of mice was pressed with a constant pressure of 450 g using a cone-shaped paw-presser with a rounded tip and immediately stopped as soon as the animal showed a struggle response, and the reaction latency was recorded in second. The analgesic effects for TASK-3 agonists were evaluated 30 min after i.p. injection.

Spontaneous pain test

After 3 days acclimation, the SNI mice were placed in an elevated transparent cage (20 × 20 × 14 cm) with a wire mesh floor (0.5 × 0.5 cm). A 5 min duration was videoed by an action camera (SONY, HDR-AS50) for each mouse, and the number of left hindpaw flinching was calculated by a blind experimenter.

Cold plantar test

Mice were allowed to acclimate to the testing environment 2-3 h daily for 3 continuous

584 days. The cold probe produced freshly with fine dry ice powder into a 5 mL syringe was
585 held against a 6 mm depth of flat glass. The center of hindpaw was targeted and the
586 withdrawal latency manifesting as quick flick or paw licking was recorded. A cutoff time
587 of 30 s was used to prevent potential tissue damage.

588 **von Frey test**

589 The SNI rats and mice were individually placed in the chamber as described in the
590 spontaneous pain test. Mechanical sensitivity was assessed by two methods:

591 Method 1 (for all the von Frey tests described except Fig. 5D): The mechanical paw
592 withdrawal threshold was assessed using von Frey filaments with an ascending order. The
593 tip of filament was perpendicularly targeted to the region comprising of the sural nerve
594 territory and sufficient stimulation was held for 1 s. Rapid paw withdrawal or flinching
595 was considered as a positive response and the bending force for which at least 60% of the
596 application elicited positive response was recorded as the mechanical paw withdrawal
597 threshold.

598 Method 2 (up-down method): Mechanical responses were tested by stimulating the
599 region comprising of the sural nerve territory with von Frey monofilaments by using the
600 up-and-down method, starting with 0.04 g. Biting, licking, and withdrawal during or
601 immediately following the 3 s stimulus were considered as a positive response.

602 **Hargreaves test**

603 The hindpaw sensitivity to thermal noxious stimulus was assessed using a radiant heat

source (model 37370; Ugo-Basile, Varese, Italy), stimulus intensity was set to produce an approximate latency of 10 s at baseline, and a cut-off value was set at 20 s to avoid unexpected damage. Mice were allowed to acclimate in Plexiglas chambers with a glass floor for 3 days, and the time to paw withdrawal was measured per mouse with a 5 min inter-stimulation period. Three trials were averaged to yield the withdrawal latency.

RNAscope *in situ* hybridization

Sequences of target probes, preamplifier, amplifier and label probes are proprietary and commercially available (Advanced Cell Diagnostics). *In situ* hybridization was performed on frozen DRG sections (10 μm) using RNAscope Multiplex Fluorescent Reagent Kit v2 (ACDbio, Cat#323100) and RNAscope 4-Plex Ancillary Kit for Multiplex Fluorescent Kit v2 (ACDbio, Cat#323120). The hybridization assay as described by vendor's protocol. *In situ* probes include: *Kcnk3* (Cat#534881), *Kcnk9* (Cat#475681), *Trpa1* (Cat#400211), *Trpv1* (Cat#313331), *Trpm8* (Cat#420451), *Rbfox3* (Cat#313311), *Th* (Cat#317621), *Ntrk2* (Cat#423611), *P2rx3* (Cat#521611). The specificity of the fluorescent signals was validated by RNAscope 3-plex Positive Control Probe (Cat#320881) and RNAscope 3-plex Negative Control Probe (Cat#320871). Fluorescent images were taken using a NIKON A1R^{+}MP Two-photon confocal scanning microscope and were analyzed using ImageJ software.

Acutely dissociated DRG neuron preparation and electrophysiology

3-6 week-old male Sprague-Dawley rats were sacrificed. The DRGs were collected in a

35-mm tissue culture dish and digested in 3% collagenase for 20 min, followed by 1% trypsin for another 30 min. After titrating by sucking up and down, the DRG neurons were cultured in Neurobasal containing 2% B27 medium for 2-4 h. The bath solution contained (in mM): 140 NaCl, 3 KCl, 1.3 $MgCl_2$, 10 HEPES, 2.4 $CaCl_2$, 10 glucose, pH 7.3. The pipette solution contained (in mM): 40 KCl, 10 HEPES, 5 EGTA, 10 NaCl, 95 K-gluconate, 4 Mg-ATP, pH 7.4. To minimize voltage-gated currents, the voltage ramps from -120 mV to -30 mV were applied, and 1mM CsCl was added extracelluarly to block hyperpolarization-activated currents. To determine the reversal potential of the CHET3-sensitive currents, NaCl was replaced with equimolar KCl. The whole-cell recordings were performed with similar hardware settings as described in electrophysiology in HEK-293 cells.

Acutely dissociated DRG neuron preparation and intracellular Ca^{2+} imaging

2 week-old male Sprague-Dawley rats were sacrificed. The DRGs were collected in a 35-mm tissue culture dish and digested in 2.5 mg/mL papain (Sigma-Aldrich) for 30 min at 37 ℃, followed by 2.5 mg/mL collagenase (Sigma-Aldrich) for another 30 min. Digested ganglia were gently washed with neurobasal medium and mechanically dissociated by passage through pipet. Neurons were seeded on laminin-coated wells (Corning) and cultured overnight at 37 ℃ in 5% CO_2 in 2% B27 (Sigma-Aldrich), supplemented neuronbasal medium, containing 50 ng/mL GDNF (PeproTech), 50 ng/mL BDNF (PeproTech).

644 Changes in intracellular Ca^{2+} concentration were monitored using ratiometric
645 Fura-2-based fluorimetry. Neurons were loaded with 2 μM Fura-2-acetoxymethyl ester
646 (Yeasen) dissolved in bath solution and 0.02% Pluronic F127 (Sigma-Aldrich) for 30 min
647 at 37℃. Fluorescence was measured during alternating illumination at 340 and 380 nm
648 using Olympus IX73 inverted fluorescence microscopy system. The bath solution
649 contained (in mM): 138 NaCl, 5.4 KCl, 2 $CaCl_2$, 2 $MgCl_2$, 10 glucose, and 10 HEPES,
650 pH 7.4, adjusted with NaOH. At the end of each experiment, cells were subjected to a
651 depolarizing solution containing 50 mM KCl, and non-responsive cells to 50 mM KCl
652 were excluded from analysis. Bar graphs in Fig. 7I and fig. S14B were pooled data from
653 both responding cells and non-responding cells in different conditions.

654 **Thermal stimulation**

655 Coverslip pieces with culture cells were placed in a recording chamber and continuously
656 perfused (about 1 mL/min).

657 Cool stimulation: the temperature was adjusted with ice bag cool perfuse solution, and
658 controlled by a feedback device. Cold sensitivity was investigated with a ~2 min duration
659 ramp-like temperature drop from 37 ℃ to ~15 ℃.

660 Heat stimulation: the temperature was adjusted with a water-heated device (model
661 TC-324B/344B, America), with the temperature of the perfuse solution raise, and
662 controlled by a feedback device. Heat sensitivity was investigated with a ~5 min duration
663 ramp-like temperature rise from 25 ℃ to ~43 ℃.

664 **Statistical analysis**

665 Statistical analyses were carried out using the Origin 9.0 software (Origin Lab
666 Corporation, Northampton, USA). Data were analyzed as described in the figure legends.
667 Normality of the data distribution was determined before appropriate statistical methods
668 were chosen. The drug was assessed as significantly active by using statistical tests
669 performed between values of the baseline and those of given time points unless specified.
670 No statistical methods were used to predetermine sample sizes.

671

672 **SUPPLEMENTARY MATERIALS**

673 Materials and Methods

674 Fig. S1. A potential druggable pocket identified in several structures of K2P channels.

675 Fig. S2. Representative current traces for whole-cell recordings on several K2P channels
676 and other ion channels.

677 Fig. S3. 10 μM CHET3 does not show effect on three pain-related GPCRs.

678 Fig. S4. Binding modes of CHET3 suggested by docking and MD simulations.

679 Fig. S5. Whole-cell path-clamp current recording for three TASK-3 mutants.

680 Fig. S6. Conformations of the extracellular ion pathway in MD simulations.

681 Fig. S7. Dose-dependent analgesia by CHET3 in mechanical allodynia.

682 Fig. S8. Effects of CHET3 on the locomotion activities, blood pressure and body
683 temperature in rodents.

REFERENCES AND NOTES

1. N. D. Volkow, A. T. McLellan, Opioid abuse in chronic pain—misconceptions and mitigation strategies. *Eur. J. Neurosci.* **374**, 1253-1263 (2016).
2. A. S. Yekkirala, D. P. Roberson, B. P. Bean, C. J. Woolf, Breaking barriers to novel analgesic drug development. *Nat. Rev. Drug Discov.* **16**, 544-563 (2017).
3. S. A. N. Goldstein, D. Bockenhauer, I. O'Kelly, N. Zilberberg, Potassium leak channels and the KCNK family of two-P-domain subunits. *Nat. Rev. Neurosci.* **2**, 175-184 (2001).
4. J. Busserolles, C. Tsantoulas, A. Eschalier, J. A. Lopez Garcia, Potassium channels in neuropathic pain: advances, challenges, and emerging ideas. *Pain* **157**, S7-S14

(2016).

5. S. G. Waxman, G. W. Zamponi, Regulating excitability of peripheral afferents: emerging ion channel targets. *Nat. Neurosci.* **17**, 153-163 (2014).
6. A. Mathie, E. L. Veale, Two-pore domain potassium channels: potential therapeutic targets for the treatment of pain. *Pflugers Arch.* **467**, 931-943 (2015).
7. Y. Kim, H. Bang, D. Kim, TASK-3, a new member of the tandem pore K^+ channel family. *J. Biol. Chem.* **275**, 9340-9347 (2000).
8. S. Rajan, E. Wischmeyer, G. X. Liu, R. P. Muller, J. Daut, A. Karschin, C. Derst, TASK-3, a novel tandem pore domain acid-sensitive K^+ channel - An extracellular histidine as pH sensor. *J. Biol. Chem.* **275**, 16650-16657 (2000).
9. T. K. Baumann, P. Chaudhary, M. E. Martenson, Background potassium channel block and TRPV1 activation contribute to proton depolarization of sensory neurons from humans with neuropathic pain. *Eur. J. Neurosci.* **19**, 1343-1351 (2004).
10. C. Morenilla-Palao, E. Luis, C. Fernández-Peña, E. Quintero, J. L. Weaver, D. A. Bayliss, F. Viana, Ion channel profile of TRPM8 cold receptors reveals a role of TASK-3 potassium channels in thermosensation. *Cell Rep.* **8**, 1571-1582 (2014).
11. D. J. Langford, C. West, C. Elboim, B. A. Cooper, G. Abrams, S. M. Paul, B. L. Schmidt, J. D. Levine, J. D. Merriman, A. Dhruva, J. Neuhaus, H. Leutwyler, C. Baggott, C. W. Sullivan, B. E. Aouizerat, C. Miaskowski, Variations in potassium channel genes are associated with breast pain in women prior to breast cancer surgery.

724 *J. Neurogenet.* **28**, 122-135 (2014).

725 12. V. Le Guilloux, P. Schmidtke, P. Tuffery, Fpocket: an open source platform for ligand
726 pocket detection. *BMC bioinformatics* **10**, 168 (2009).

727 13. A. N. Miller, S. B. Long, Crystal structure of the human two-pore domain potassium
728 channel K2P1. *Science* **335**, 432-436 (2012).

729 14. M. Lolicato, P. M. Riegelhaupt, C. Arrigoni, K. A. Clark, D. L. Minor, Jr.,
730 Transmembrane helix straightening and buckling underlies activation of
731 mechanosensitive and thermosensitive K2P channels. *Neuron* **84**, 1198-1212 (2014).

732 15. Y. Y. Dong, A. C. Pike, A. Mackenzie, C. McClenaghan, P. Aryal, L. Dong, A.
733 Quigley, M. Grieben, S. Goubin, S. Mukhopadhyay, G. F. Ruda, M. V. Clausen, L.
734 Cao, P. E. Brennan, N. A. Burgess-Brown, M. S. Sansom, S. J. Tucker, E. P.
735 Carpenter, K2P channel gating mechanisms revealed by structures of TREK-2 and a
736 complex with Prozac. *Science* **347**, 1256-1259 (2015).

737 16. F. Sievers, A. Wilm, D. Dineen, T. J. Gibson, K. Karplus, W. Li, R. Lopez, H.
738 McWilliam, M. Remmert, J. Soding, J. D. Thompson, D. G. Higgins, Fast, scalable
739 generation of high-quality protein multiple sequence alignments using Clustal
740 Omega. *Mol. Syst. Biol.* **7**, 539 (2011).

741 17. S. F. Altschul, T. L. Madden, A. A. Schäffer, J. Zhang, Z. Zhang, W. Miller, D. J.
742 Lipman, Gapped BLAST and PSI-BLAST: a new generation of protein database
743 search programs. *Nucleic Acids Res.* **25**, 3389-3402 (1997).

744 18. M. Bertoni, F. Kiefer, M. Biasini, L. Bordoli, T. Schwede, Modeling protein
745 quaternary structure of homo- and hetero-oligomers beyond binary interactions by
746 homology. *Sci Rep.* **7**, 10480 (2017).
747 19. A. Waterhouse, M. Bertoni, S. Bienert, G. Studer, G. Tauriello, R. Gumienny, F. T.
748 Heer, T. A. P. de Beer, C. Rempfer, L. Bordoli, R. Lepore, T. Schwede,
749 SWISS-MODEL: homology modelling of protein structures and complexes. *Nucleic*
750 *Acids Res.* **46**, W296-W303 (2018).
751 20. A. Šali, T. L. Blundell, Comparative protein modelling by satisfaction of spatial
752 restraints. *J. Mol. Biol.* **234**, 779-815 (1993).
753 21. C. A. Coburn, Y. F. Luo, M. X. Cui, J. B. Wang, R. Soll, J. C. Dong, B. Hu, M. A.
754 Lyon, V. P. Santarelli, R. L. Kraus, Y. Gregan, Y. Wang, S. V. Fox, J. Binns, S. M.
755 Doran, D. R. Reiss, P. L. Tannenbaum, A. L. Gotter, P. T. Meinke, J. J. Renger,
756 Discovery of a pharmacologically active antagonist of the two-pore-domain
757 potassium channel K_{2P}9.1 (TASK-3). *ChemMedChem* **7**, 123-133 (2012).
758 22. G. Czirják, P. Enyedi, Formation of functional heterodimers between the TASK-1
759 and TASK-3 two-pore domain potassium channel subunits. *J. Biol. Chem.* **277**,
760 5426-5432 (2002).
761 23. C. E. Clarke, E. L. Veale, P. J. Green, H. J. Meadows, A. Mathie, Selective block of
762 the human 2-P domain potassium channel, TASK-3, and the native leak potassium
763 current, IK_{SO}, by zinc. *J. Physiol.* **560**, 51-62 (2004).

764 24. S. Rinné, A. K. Kiper, G. Schlichthörl, S. Dittmann, M. F. Netter, S. H. Limberg, N.
765 Silbernagel, M. Zuzarte, R. Moosdorf, H. Wulf, E. Schulze-Bahr, C. Rolfes, N. Decher,
766 TASK-1 and TASK-3 may form heterodimers in human atrial cardiomyocytes. *J. Mol.*
767 *Cell. Cardiol.* **81**, 71-80 (2015).
768 25. M. Schewe, H. Sun, Ü. Mert, A. Mackenzie, A. C. W. Pike, F. Schulz, C. Constantin,
769 K. S. Vowinkel, L. J. Conrad, A. K. Kiper, W. Gonzalez, M. Musinszki, M. Tegtmeier,
770 D. C. Pryde, H. Belabed, M. Nazare, B. L. de Groot, N. Decher, B. Fakler, E. P.
771 Carpenter, S. J. Tucker, T. Baukrowitz, A pharmacological master key mechanism
772 that unlocks the selectivity filter gate in K^+ channels. *Science* **363**, 875-880 (2019).
773 26. I. W. Davis, D. Baker, RosettaLigand docking with full ligand and receptor flexibility.
774 *J. Mol. Biol.* **385**, 381-392 (2009).
775 27. G. Lemmon, J. Meiler, Rosetta Ligand docking with flexible XML protocols.
776 *Methods Mol. Biol.* **819**, 143-155 (2012).
777 28. W. González, L. Zúñiga, L. P. Cid, B. Arévalo, M. I. Niemeyer, F. V. Sepúlveda, An
778 extracellular ion pathway plays a central role in the cooperative gating of a K2P K^+
779 channel by extracellular pH. *J. Biol. Chem.* **288**, 5984-5991 (2013).
780 29. F. V. Abbott, K. B. Franklin, R. F. Westbrook, The formalin test: scoring properties of
781 the first and second phases of the pain response in rats. *Pain* **60**, 91-102 (1995).
782 30. A. Tappe-Theodor, R. Kuner, Studying ongoing and spontaneous pain in
783 rodents-challenges and opportunities. *Eur. J. Neurosci.* **39**, 1881-1890 (2014).

784 31. E. Navratilova, F. Porreca, Reward and motivation in pain and pain relief. *Nat. Rev.*
785 *Neurosci.* **17**, 1304-1312 (2014).
786 32. L. A. McWilliams, B. J. Cox, M. W. Enns, Mood and anxiety disorders associated
787 with chronic pain: an examination in a nationally representative sample. *Pain* **106**,
788 127-133 (2003).
789 33. P. J. Turner, K. J. Buckler, Oxygen and mitochondrial inhibitors modulate both
790 monomeric and heteromeric TASK-1 and TASK-3 channels in mouse carotid body
791 type-1 cells. *J. Physiol.* **591**, 5977-5998 (2013).
792 34. J. Vriens, B. Nilius, T. Voets, Peripheral thermosensation in mammals. *Nat. Rev.*
793 *Neurosci.* **15**, 573-589 (2014).
794 35. L. Li, M. Rutlin, V. E. Abraira, C. Cassidy, L. Kus, S. Gong, M. P. Jankowski, W.
795 Luo, N. Heintz, H. R. Koerber, C. J. Woodbury, D. D. Ginty, The functional
796 organization of cutaneous low-threshold mechanosensory neurons. *Cell* **147**,
797 1615-1627 (2011).
798 36. L. Vulchanova, M. S. Riedl, S. J. Shuster, L. S. Stone, K. M. Hargreaves, G. Buell, A.
799 Surprenant, R. A. North, R. Elde, P2X3 is expressed by DRG neurons that terminate
800 in inner lamina II. *Eur. J. Neurosci.* **10**, 3470-3478 (1998).
801 37. S. L. Pollema-Mays, M. V. Centeno, C. J. Ashford, A. V. Apkarian, M. Martina,
802 Expression of background potassium channels in rat DRG is cell-specific and
803 down-regulated in a neuropathic pain model. *Mol. Cell. Neurosci.* **57**, 1-9 (2013).

804 38. J. R. Deuis, Z. Dekan, J. S. Wingerd, J. J. Smith, N. R. Munasinghe, R. F. Bhola, W.
805 L. Imlach, V. Herzig, D. A. Armstrong, K. J. Rosengren, F. Bosmans, S. G. Waxman,
806 S. D. Dib-Hajj, P. Escoubas, M. S. Minett, M. J. Christie, G. F. King, P. F. Alewood,
807 R. J. Lewis, J. N. Wood, I. Vetter, Pharmacological characterisation of the highly
808 $Na_V1.7$ selective spider venom peptide Pn3a. *Sci Rep.* **7**, 40883 (2017).
809 39. E. C. Emery, A. P. Luiz, J. N. Wood, $Na_v1.7$ and other voltage-gated sodium channels
810 as drug targets for pain relief. *Expert Opin. Ther. Targets* **20**, 975-983 (2016).
811 40. P. Royal, A. Andres-Bilbe, P. Á. Prado, C. Verkest, B. Wdziekonski, S. Schaub, A.
812 Baron, F. Lesage, X. Gasull, J. Levitz, G. Sandoz, Migraine-associated TRESK
813 mutations increase neuronal excitability through alternative translation initiation and
814 inhibition of TREK. *Neuron* **101**, 232-245 (2019).
815 41. D. W. Kang, J. H. Han, E. M. Talley, D. A. Bayliss, D. H. Kim, Functional expression
816 of TASK-1/TASK-3 heteromers in cerebellar granule cells. *J. Physiol.* **554**, 64-77
817 (2004).
818 42. A. P. Berg, E. M. Talley, J. P. Manger, D. A. Bayliss, Motoneurons express
819 heteromeric TWIK-related acid-sensitive K^+ (TASK) channels containing TASK-1
820 (KCNK3) and TASK-3 (KCNK9) subunits. *J. Neurosci.* **24**, 6693-6702 (2004).
821 43. D. Kim, E. J. Cavanaugh, I. Kim, J. L. Carroll, Heteromeric TASK-1/TASK-3 is the
822 major oxygen-sensitive background K^+ channel in rat carotid body glomus cells. *J.*
823 *Physiol.* **587**, 2963-2975 (2009).

824 44. S. Pronk, S. Páll, R. Schulz, P. Larsson, P. Bjelkmar, R. Apostolov, M. R. Shirts, J. C.
825 Smith, P. M. Kasson, D. van der Spoel, B. Hess, E. Lindahl, GROMACS 4.5: a
826 high-throughput and highly parallel open source molecular simulation toolkit.
827 *Bioinformatics* **29**, 845-854 (2013).
828 45. J. B. Klauda, R. M. Venable, J. A. Freites, J. W. O'Connor, D. J. Tobias, C.
829 Mondragon-Ramirez, I. Vorobyov, A. D. MacKerell, Jr., R. W. Pastor, Update of the
830 CHARMM all-atom additive force field for lipids: validation on six lipid types. *J.*
831 *Phys. Chem. B* **114**, 7830-7843 (2010).
832 46. P. V. Bharatam, D. S. Patel, P. Iqbal, Pharmacophoric features of biguanide
833 derivatives: an electronic and structural analysis. *J. Med. Chem.* **48**, 7615-7622
834 (2005).
835 47. K. M. Tye, R. Prakash, S. Y. Kim, L. E. Fenno, L. Grosenick, H. Zarabi, K. R.
836 Thompson, V. Gradinaru, C. Ramakrishnan, K. Deisseroth, Amygdala circuitry
837 mediating reversible and bidirectional control of anxiety. *Nature* **471**, 358-362
838 (2011).

839

840 **Acknowledgements:** We thank Bioray Laboratories for technical support in preparing
841 *Kcnk9* knockout mice. We thank Dr. Tao Li (West China Hospital) for technical assistance
842 with blood pressure test and Miss Rongrong Cui (SIMM) for assistance on PK test. We
843 thank the supports of ECNU Multifunctional Platform for Innovation (001 and 011).

Funding: This work was funded by National Science & Technology Major Project "Key New Drug Creation and Manufacturing Program" of China (2018ZX09711002 to H.J., Q.Z., and H.Y.), the National Natural Science Foundation of China (21422208 to H.Y; 31600832 to R.J.), Thousand Talents Plan in Sichuan Province (to R.J.), 1.3.5 Project for Disciplines of Excellence (ZY2016101), West China Hospital, Sichuan University (to J.L.), the "XingFuZhiHua" funding of ECNU (44300-19311-542500/006), the Fundamental Research Funds for the Central Universities (to H.Y., and 2018SCUH0086 to R.J.) and the Special Program for Applied Research on Super Computation of the NSFC-Guangdong Joint Fund (the second phase) under Grant No.U1501501, and the State Key Laboratory of Bioorganic and Natural Products Chemistry. **Author contributions:** P.L. performed behavior tests, ISH, Ca^{2+} imaging; Y.Q. performed drug design and computations; Y.M. performed mouse genetics on TASK-3 KO mice and behavior tests; J.F. performed electrophysiology; Z.S. performed electrophysiology, behavior tests, ISH; L.H. performed electrophysiology; S.B., Y.W. and B.S. performed Ca^{2+} imaging; J.Z. and W.G.L. performed elevated plus maze tests; Z.C. and N.P. assisted with behavior tests and cell culture; E.S. performed dark/light box tests; L.Y. assisted with behavior tests; F.T., X.L. and Z.G. performed electrophysiology for some of the initial compound screenings; P.S., Y.C. and Y.M. performed pharmacokinetics study; D.H. performed the qPCR experiments for TASK-3 KO mice; L.Z. performed experiments of μOR; D.Y. performed experiments of 5-HT_{1B}R; W.L. performed experiments of CB_1R;

T.Y., J.X. and Y.M. performed experiments of echocardiography. Q.Z. prepared the derivatives of CHET3. J.L. oversaw the animal behavior tests. H.J. oversaw the computations. R.J. and H.Y. initiated, supervised the project, analyzed the experiments, and wrote the manuscript with input from all co-authors. **Competing interests:** The authors declare no competing interests. **Data and materials availability:** All data is available in the main text or the supplementary materials.

Figures

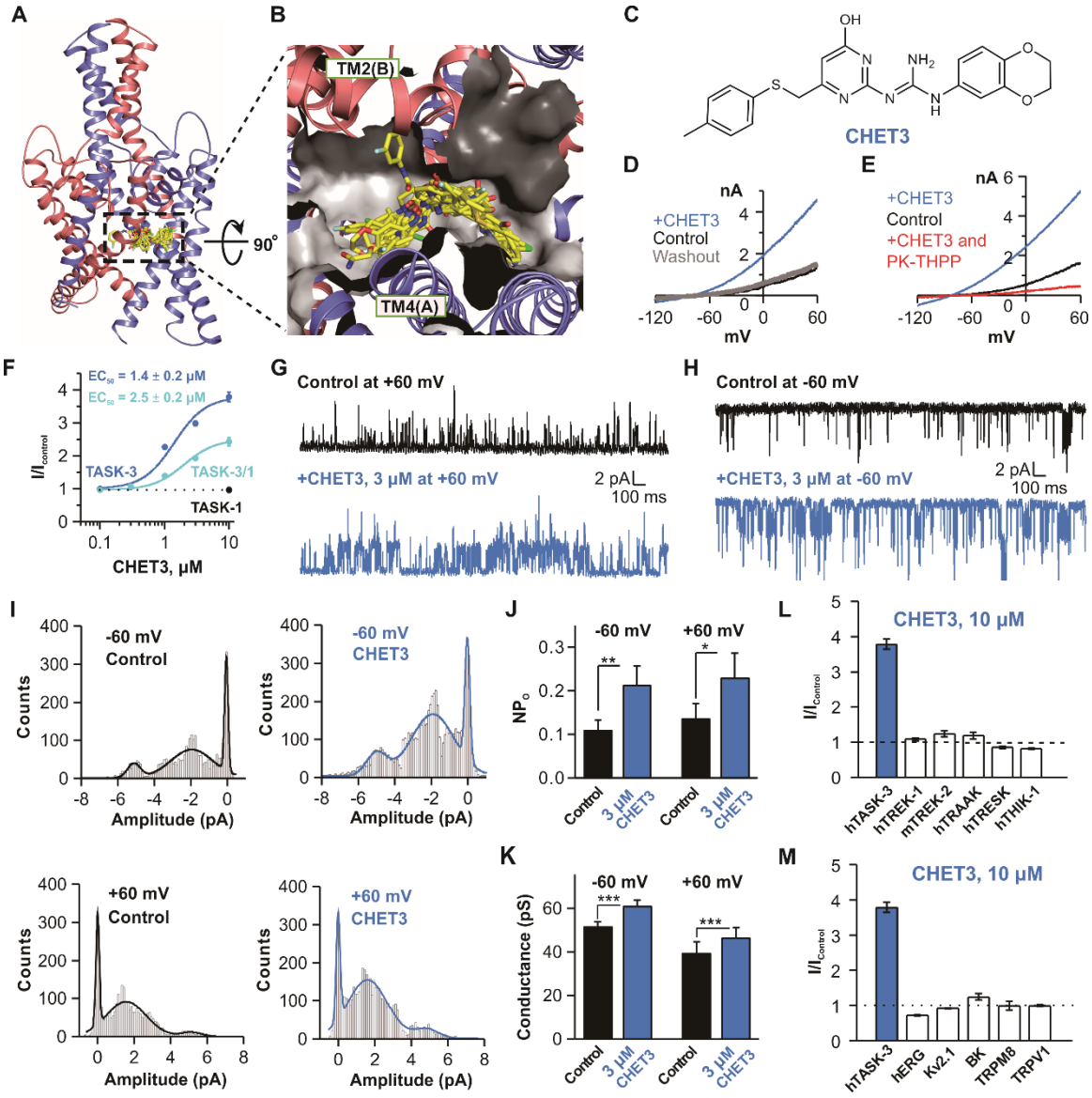

872

873 **Fig. 1. Structure-based ligand discovery of CHET3.**

874 (**A**) Pocket in a TASK-3 homology model used for virtual screening. Representative
875 docking poses were shown. **(B)** Cytoplasmic expanded view of the pocket and the
876 docking poses. (**C**) Chemical structure of CHET3. (**D** and **E**) Exemplar whole-cell
877 path-clamp recordings showing the activation of TASK-3 by 10 µM CHET3 and
878 blockade of 0.5 µM PK-THPP. (**F**) CHET3 dose-response curves for TASK-3 (n = 7) and

879 TASK-3/TASK-1 (n = 5). (**G** and **H**) Representative single-channel current traces from
880 inside-out patches showing the activation of TASK-3 by CHET3 at +60 mV (G) and -60
881 mV (H). (**I**) Histograms of the single-channel currents which were fitted by Gaussian
882 distributions. (**J** and **K**) Analysis of NP_o (channel number times open probability)
883 changes and conductance changes from the single-channel currents (n = 6; paired *t* test).
884 (**L**) Summary for the effects of CHET3 on several other K2P channels (n = 7-10). (**M**)
885 Summary for the effects of CHET3 on hERG, Kv2.1, BK, TRPM8 and TRPV1 channels
886 (n = 5-7). Data in (F, J to M) are shown as mean ± SEM. **P* < 0.05, ***P* < 0.01, ****P* <
887 0.001.
888
889
890
891

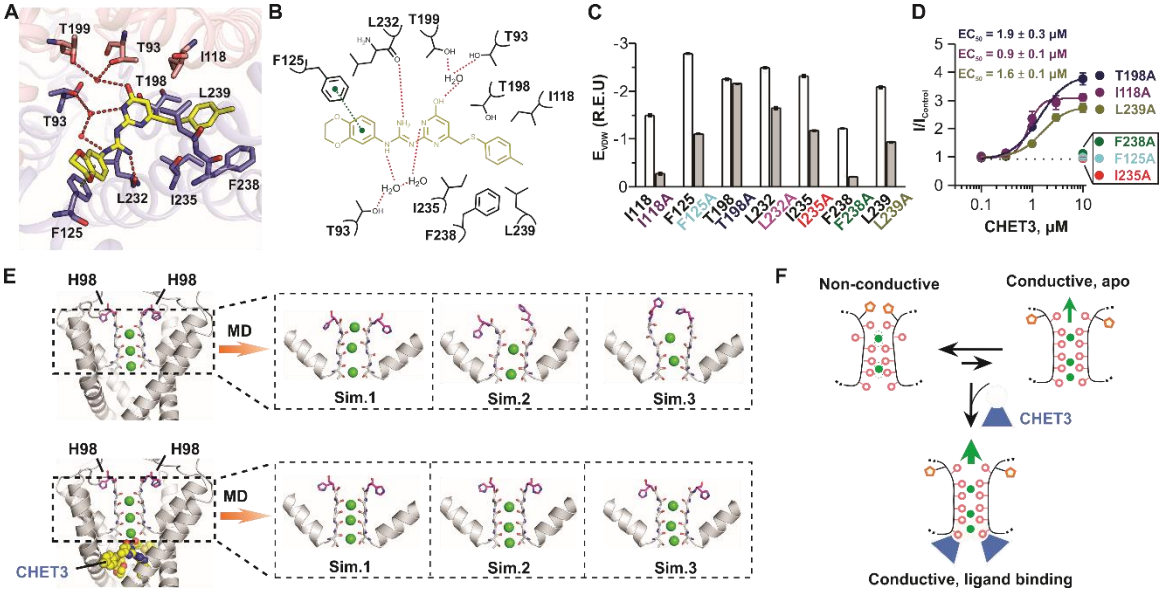

892

Fig. 2. Activation mechanism of CHET3 on TASK-3.

(**A** and **B**) 3-dimentional and 2-dimentional diagrams showing interactions between CHET3 and TASK-3. Hydrogen bond (red dash) and π-π interaction (green dash) were shown. (**C**) Computations showing the contributions of seven residues and their mutations to CHET3 binding. Energy unit is Rosetta Energy Unit (R.E.U.). (**D**) Dose-response curves of six mutations on CHET3 activity (n = 6). Data are shown as mean ± SEM. (**E**) Selectivity filter conformations of the *apo* TASK-3 and the CHET3-bound TASK-3 revealed by MD simulations, including bound potassium ions (green spheres), carbonyl oxygen (red sphere) rotation of filter residues, and movements of residue H98 (purple sticks). (**F**) Schematic representation of the action mechanism of CHET3 on TASK-3.

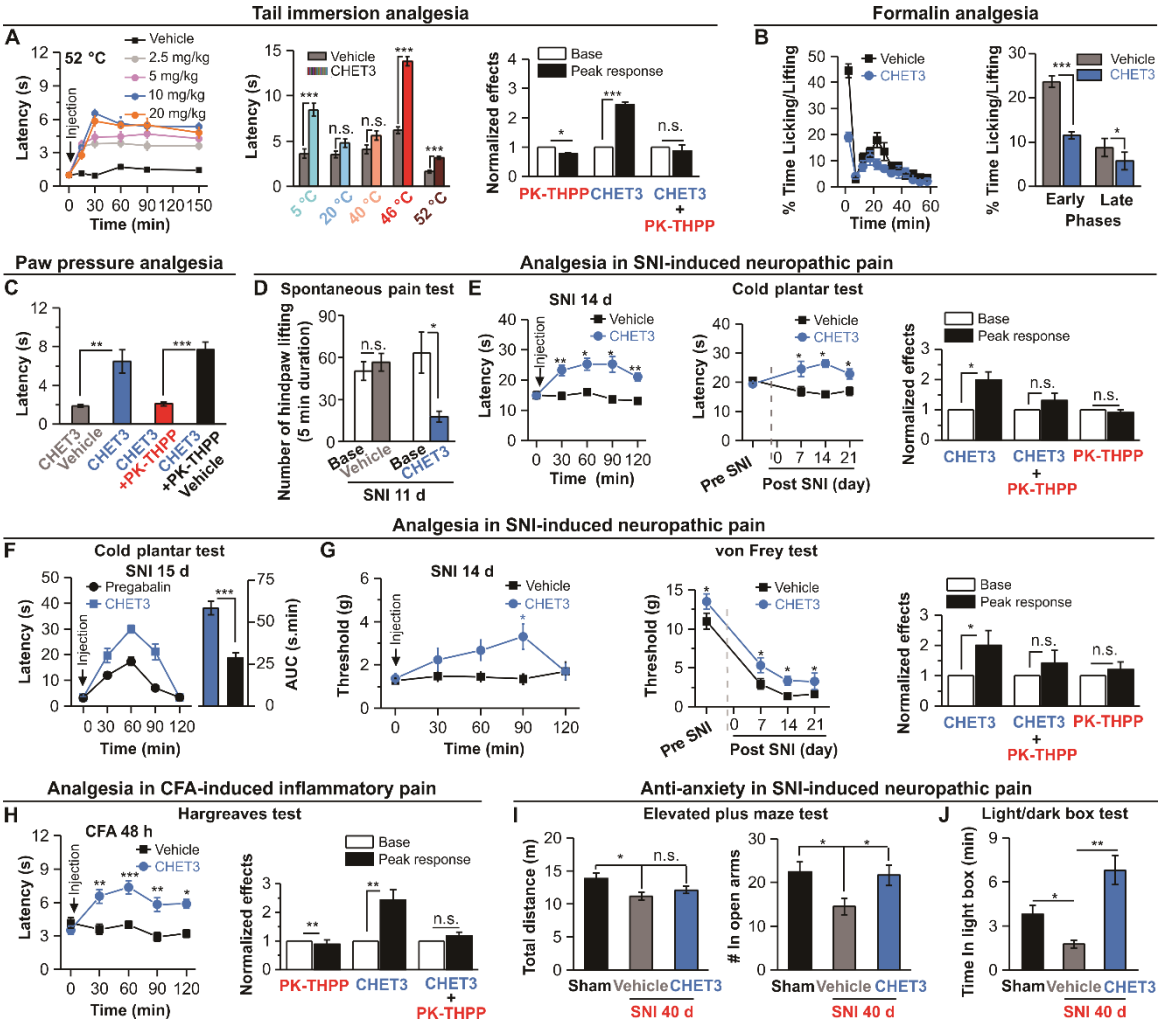

Fig. 3. Analgesic effects of CHET3 in rodents.

(**A**) *left*, Time profile for dose-dependent analgesia by CHET3 in tail immersion test at 52 °C (n = 6-10); *middle*, CHET3 analgesia in tail immersion tests at different temperatures (n = 9-11; unpaired *t* test); *right*, Summary for PK-THPP effects (n = 8-10; unpaired *t* test). (**B**) Summary for CHET3 analgesia in formalin (2.5%, 20 μl) test (n = 8; unpaired *t* test). (**C**) CHET3 and PK-THPP on the paw withdrawal latency in paw pressure test (measured at 45 min post injection, n = 8-10; paired *t* test). (**D**) CHET3 on spontaneous pain within a 10 min duration in mice (measured at 35 min post injection, n

914 = 6-10; unpaired *t* test). (**E**) *left*, Time profile for CHET3 on cold hyperalgesia in mice (n
915 = 10-11; paired *t* test); *middle*, Summary for CHET3 on cold hyperalgesia at different
916 stages in SNI (n = 9-11; unpaired *t* test); *right*, Summary for PK-THPP (n = 10; paired *t*
917 test). (**F**) Comparison of CHET3 and Pregabalin (30 mg/kg, i.p.) in cold plantar test in
918 mice (n =11-12; unpaired *t* test). (**G**) *left*, Time profile for CHET3 in mechanical
919 allodynia in rats (n = 8-13; paired *t* test); *middle*, Summary for CHET3 on mechanical
920 allodynia at different stages in SNI rats (n = 8-13; paired *t* test); *right*, Summary for
921 PK-THPP effects (n = 8; paired *t* test). (**H**) *left*, Time profile for CHET3 on heat
922 hyperalgesia (n = 10-11; paired *t* test); *right*, Summary for PK-THPP effects (n = 11;
923 paired *t* test). (**I** and **J**) CHET3 on anxiety-like behaviors in elevated plus maze test (I) (n
924 = 8-9; unpaired *t* test) and in light/dark box tested (J) (n = 6-8; unpaired *t* test). CHET3
925 (10 mg/kg) and PK-THPP (15 mg/kg) were administrated via i.p. injections unless
926 specified. Data are shown as mean ± SEM. $*P < 0.05$, $**P < 0.01$, $***P < 0.001$. n.s.,
927 not significant.
928
929

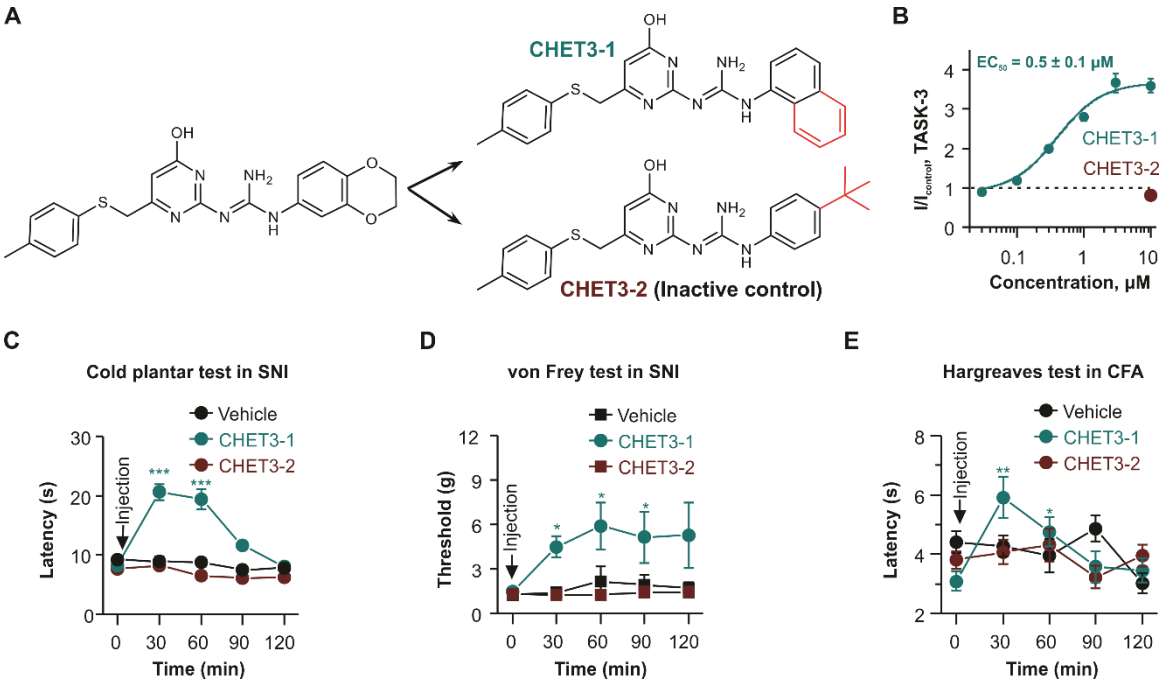

930

931 **Fig. 4. Validation of TASK-3 as analgesic target by using CHET3 derivatives.**

932 (**A**) Chemical structures of CHET3 derivatives. (**B**) Dose-response relationships for

933 CHET3-1 (n = 6) and CHET3-2 (n = 7) on TASK-3. (**C** to **E**) CHET3-1 and CHET3-2 in

934 cold hyperalgesia (C) (n = 9-11; paired *t* test), mechanical allodynia (D) (n = 7-8; paired *t*

935 test), and heat hyperalgesia (E) (n = 9-10; paired *t* test). Data are shown as mean ± SEM.

936 **P* < 0.05, ***P* < 0.01, ****P* < 0.001.

937

938

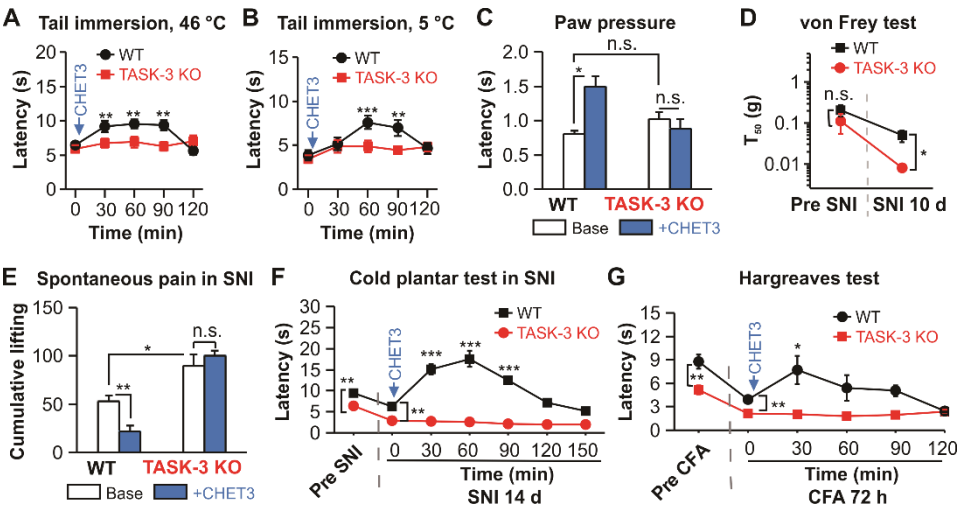

Fig. 5. Effects of systemic administration of CHET3 on TASK-3 KO mice.

(**A** and **B**) CHET3 had no analgesic effects in tail immersion tests in TASK-3 KO mice (n = 9-12; paired *t* test). (**C**) CHET3 had no analgesic effect in paw pressure tests in TASK-3 KO mice (n = 8 for KO, n = 7 for WT; paired *t* test). Note that no change of baseline sensitivity in nociception for TASK-3 KO mice in A to C. (**D**) TASK-3 KO mice in SNI model exhibited enhanced mechanical allodynia (up-down method, n = 8 for KO, n = 10 for WT; unpaired *t* test). (**E**) TASK-3 KO mice in SNI model exhibited enhanced spontaneous pain activities which was insensitive to CHET3 (n = 6-7; paired *t* test). (**F** and **G**) CHET3 had no analgesic effect in cold plantar test (n = 6-7; paired *t* test) in SNI model and Hargreaves test (n = 8-12; paired *t* test) in CFA model in TASK-3 KO mice. Note that TASK-3 KO mice had shorter paw withdraw latencies in both tests (unpaired *t* test) in base conditions. Data are shown as mean ± SEM. **P* < 0.05, ***P* < 0.01, ****P* < 0.001. n.s., not significant.

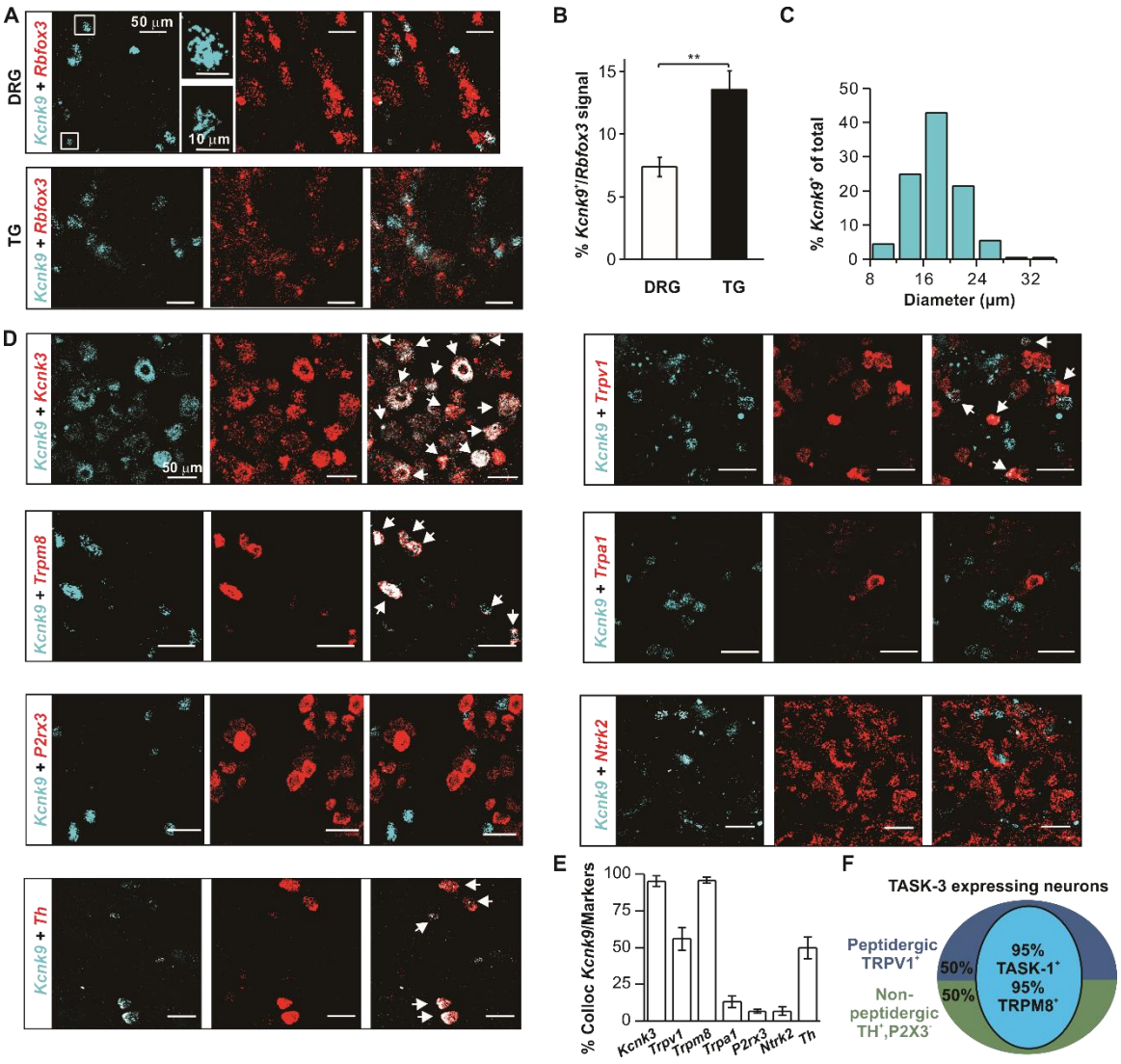

954

955 **Fig 6. Distribution of TASK-3 in DRG neurons.**

956 (**A** and **B**) Images and quantifications showing *Kcnk9* expression in sensory neurons

957 using RNAscope (n = 7 sections from 3 mice) and TG (n = 8 sections from 3 mice)

958 (Mann-Whitney test). Data in (B) are shown as mean ± SEM. (**C**) Quantification of the

959 cell sizes of *Kcnk9*$^{+}$ neurons (n = 6 sections from 3 mice). (**D**) Representative images

960 showing *Kcnk9*$^{+}$ neurons expression in different subtype of DRG neurons using

961 RNAscope. (**E**) Bar graph summary for experiments in (D) (n = 4-9 DRG sections from

962 3-8 mice for each condition). Data are shown as mean ± SEM. (**F**) Schematic summary

963 for the distribution of *Kcnk9*$^{+}$ neurons in DRG. $^{**}P < 0.01$.

964

965

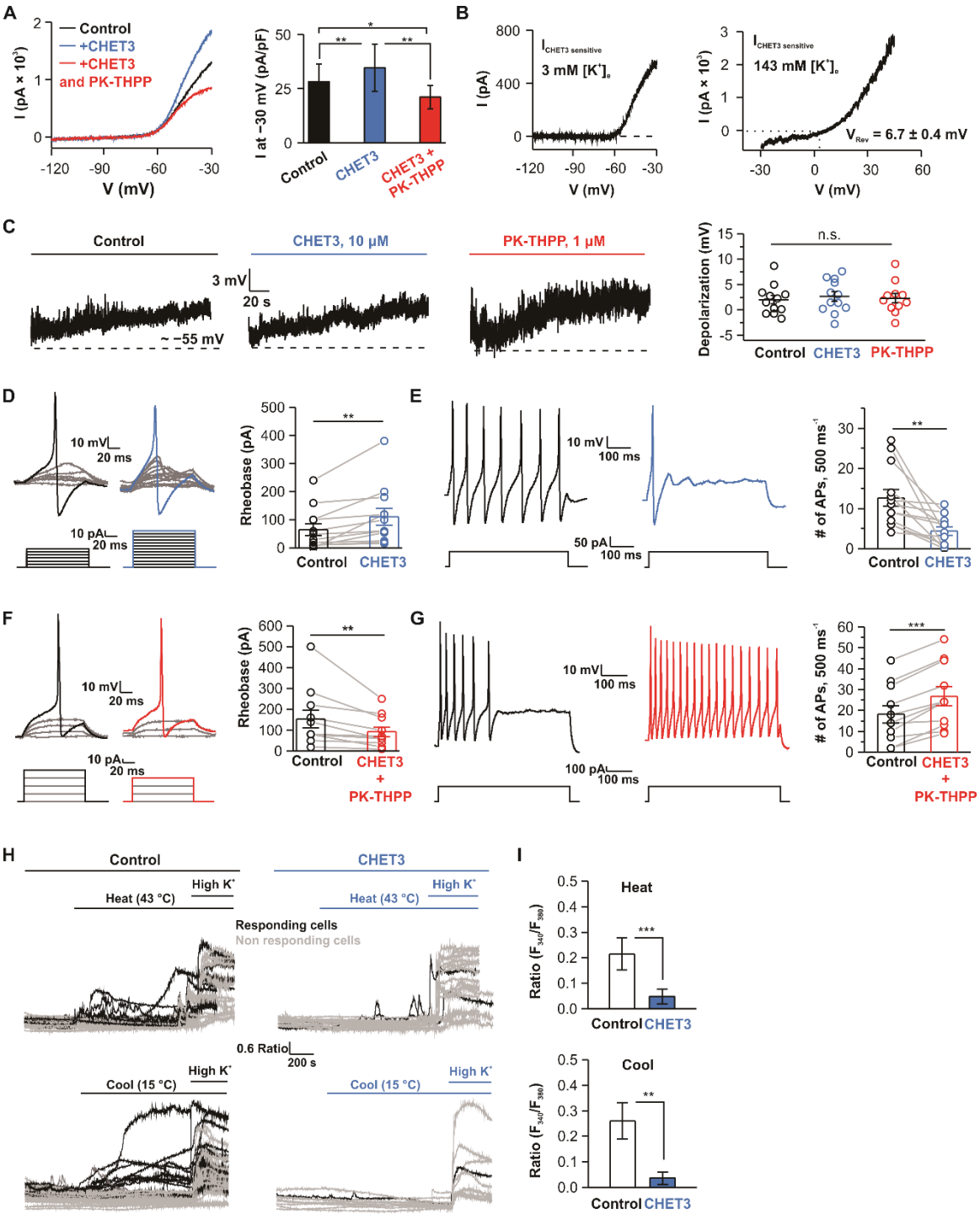

966

967 **Fig 7. Functional roles of TASK-3 in nociceptive neurons.**

968 (**A**) *left*, Representative electrophysiological traces showing CHET3 (10 µM) and

969 PK-THPP (1 µM) effects on K^+ currents in DRG neurons; *right*, Bar graph summary for

970 experiments in *left* (n = 9 cells in 6 mice; paired *t* test). (**B**) Representative traces showing
971 CHET3-sensitive currents at different extracellular K^+ concentrations (V_{Rev} was
972 determined from n = 5 cells in 3 mice). (**C**) Representative traces and scatter plots
973 showing resting membrane potential (RMP) changes in response to Vehicle, CHET3 or
974 PK-THPP (n = 12 cells for Control and CHET3, n = 11 cells for PK-THPP in 5 mice for
975 each condition; one-way ANOVA test). (**D** and **E**) Traces and bar graph showing CHET3
976 effect on rheobase and firing frequency in nociceptive neurons (n = 12 cells in 5 mice;
977 paired sample Wilcoxon signed rank test in (D), paired *t* test in (E)). (**F** and **G**) Traces and
978 bar graph showing co-application of CHET3 and PK-THPP on rheobase and firing
979 frequency in nociceptive neurons (n = 11 cells in 3 mice; paired sample Wilcoxon signed
980 rank test in (F), paired *t* test in (G)). (**H**) Individual Ca^{2+} imaging traces from small-sized
981 DRG neurons in representative field of views in response to heat (25 ℃-43 ℃) , cooling
982 (37 ℃-15 ℃). (**I**) Bar graphs summary for experiments in (H) (Heat: n = 143 cells in 11
983 coverslips for control, n = 99 cells in 9 coverslips for CHET3; Mann-Whitney test. Cool:
984 n = 87 cells in 9 coverslips for control, n = 46 cells in 9 coverslips for CHET3;
985 Mann-Whitney test. Both experiments were from 3 independent preparations from 6
986 mice). Data are shown as mean ± SEM. **P* < 0.05, ***P* < 0.01, ****P* < 0.001. n.s., not
987 significant.
988
989